Electronic Supplementary Material (ESI) for Soft Matter.

Supporting Information: Small-volume extensional rheology of concentrated protein and protein-excipient solutions

Kathleen T. Lauser, Amy Rueter, and Michelle A. Calabrese*

Department of Chemical Engineering and Materials Science

University of Minnesota, Minneapolis, Minnesota, 55455

*Email: mcalab@umn.edu

SI.1 Estimated Ohnesorge and Bond numbers

The dimensionless Ohnesorge number quantifies viscous forces to inertial and surface tension forces and dictates the dominant flow regime:

$$Oh = \frac{\mu}{\sqrt{\rho \sigma R_0}} \tag{SI.1.1}$$

where μ, ρ, σ and R_0 are the dynamic viscosity, density, surface tension and nozzle outer radius.

Estimated Oh for materials studied in this work are shown below in Table S1. Due to volume constraints, measurement difficulties, and that Oh was expected to be far less than unity in all cases, shear viscosities for concentrated OVA solutions were estimated using Monkos et al.,[1] which used slightly higher OVA content than seen in this work. The viscosity of dilute OVA (OVA45) was estimated using values from Brust et al.[2] on 45 mg/mL bovine serum albumin (BSA), a protein slightly larger than OVA within the same protein family (albumins). Due to these differences, Oh was estimated for the concentrations used in refs.[1,2] and was also linearly interpolated to the concentrations used in this work; both calculations are listed in Table S1. The viscosity for P188-50 was estimated from our prior work, McCauley et al.,[3] which showed little difference between viscosities at equivalent conditions for various poloxamers. While μ for most poloxamers with higher unimer contents ranged from 0.003–0.004 Pa·s, the value chosen of 0.005 Pa·s is an overestimate because a population of entirely unimers is expected at this temperature.[4] As expected, all Oh were below 1, indicating that inertia and surface tension dominate viscous forces in these systems.

Table S1: Estimated Oh and Bo for various water, OVA and P188 samples. Viscosity values marked with † are from Monkos et al.,[1] †† Brust et al.,[2] and * from McCauley et al.[3] Values of R^* are calculated based on a critical Bond number of Bo^*=0.2, as done in prior work.[5]

sample	μ [Pa · s]	Oh	Bo	R^* [mm]
Water	$8.90{\cdot}10^{-4}$	0.004	0.05	1.22
OVA45	$1.24{\cdot}10^{-3\dagger\dagger}$	0.007	0.08	1.08
OVA100	$2.81{\cdot}10^{-3}$	0.02	0.08	0.98
OVA200	$5.66{\cdot}10^{-3}$	0.03	0.09	0.93
OVA247	$7.00{\cdot}10^{-3\dagger}$	0.04	0.09	0.93
OVA300	$1.34{\cdot}10^{-2}$	0.08	0.09	0.92
OVA371	$2.20{\cdot}10^{-2\dagger}$	0.14	0.09	0.92
P188-50	$5{\cdot}10^{-3}$ *	0.03	0.09	0.94
P188-200	$1.44{\cdot}10^{-2}$	0.09	0.09	0.92

Finally, the viscosity of the 200 mg/mL P188 solution (P188-200) was measured on an Anton Paar MCR 302 stress-controlled rheometer using a 26.7 mm double-gap geometry. As these solutions are low viscosity and are expected to be nearly-Newtonian at room temperature (below the CMT), the solutions were measured at several shear rates, with higher shear rates giving an improved torque signal. Fig. S1 summarizes these findings, where error bars represent the standard deviation of the steady shear viscosity measurement in time. The shear rate $\dot{\gamma} = 0.2$ s^{-1} was at the lower torque signal limit of the rheometer, which is unsurprising given the large standard deviation shown for this shear rate in Fig. S1. While a true 'zero-shear' viscosity could not be extracted this way, the results shown in Fig. S1 indicate that the viscosities are shear-rate independent within the measurement uncertainty, confirming that solutions act nearly Newtonian over the measured shear rates.

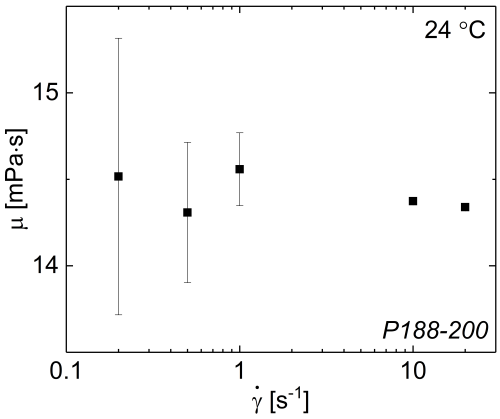

Figure S1: Shear viscosity μ at various shear rates for P188-200 at 24 °C. Error bars are the standard deviation of steady state μ values, measured over 200 s.

The dimensionless Bond number compares the importance of gravitational vs. surface tension forces. The Bond number is shown below:

$$\mathrm{Bo} = \frac{\Delta\rho g R_0^2}{\sigma} \tag{SI.1.2}$$

where $\Delta\rho$ is the difference in density between air and the liquid. Large Bond numbers indicate gravitational forces dominate while small Bond numbers indicate that gravitational forces are relatively unimportant compared to surface tension forces. $Bo < 1$ for all materials studied, which supports the importance of surface tension measurements prior to DoS experiments.

Additionally, a critical Bond number, Bo^*, is defined following Equation SI.1.2, instead using a critical radius R^* in the place of R_0. This critical Bond number indicates the point at which effects from gravitational sagging are no longer significant in the thinning process, where typically $Bo^* \leq 0.2$.[5] Thus for radii at and below the critical R^*, gravitational effects are negligible; R^* values in Table S1 are all greater than R_0. Additionally, to exclude possible gravitational effects at the onset of thinning (see Fig. 3), n_0 fits do not include very early thinning times.

SI.2 Gel electrophoresis confirmation of OVA purity

The purity of the as-received OVA was reported to be ≥98% by Sigma Aldrich agarose gel electrophoresis. Sodium dodecyl sulfate–polyacrylamide gel electrophoresis (SDS-PAGE) was performed to confirm the purity of OVA (Fig. S2). Gel electrophoresis was stopped when the dye front reached the lowest rung of the protein ladder (10 kDa). Two bands appeared at 45.5 kDa (62% of total intensity) and 39.0 (38% of total intensity). Based on the molecular weight, both bands are likely OVA, which has a molar mass of 44 kDa. The appearance of the second band is likely not an impurity but a double band of OVA that commonly occurs when using 2-mercaptoethanol as a reducing agent.[6,7] Common impurities in OVA are other egg white proteins[8–15]: ovomucoid (28 kDa), ovotransferrin (76 kDa), ovomucin (165 kDa), and lysozyme (14 kDa). A faint band appears to be visible between 70-100 kDa, which could possible be trace ovotransferrin; however this band was not distinct enough to be detected or quantified by the ImageLab analysis program. No other bands were found, indicating high OVA purity.

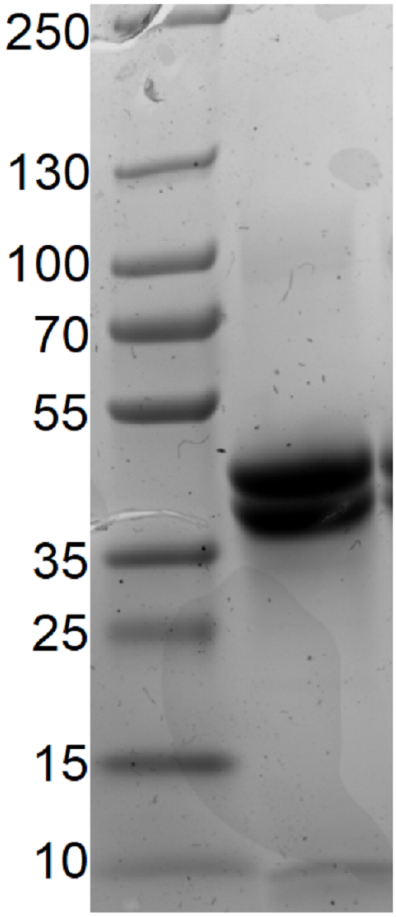

Figure S2: SDS-PAGE of a protein ladder (left) and a sample of 3 mg/mL OVA (right).

SI.3 PEO validation of direct mount DoS

To support DoS device validation, an additional PEO concentration of 0.3% wt. was explored. A representative trial is shown in Fig S3. When the radial decay is fit to the expression for EC thinning, a relaxation time of λ_E=3.43 ms is obtained. This compares favorably with the relaxation time of 3.34 ms obtained by Dinic for the same concentration solution,[16] further supporting the validity of our DoS instrument.

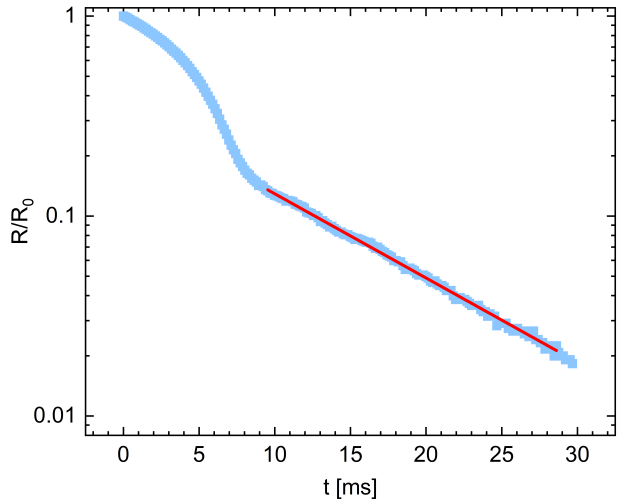

Figure S3: Radial decay of 0.3% wt PEO solution. The fit to Eqn. 2 (red) is used to extract λ_E.

SI.4 Effect of contact angle, θ

The solid-liquid interfacial energy, σ_{ls}, dictates the droplet spreading upon contact with the substrate, given by Young's Equation:

$$\sigma_{ls} = \sigma_s - \sigma_l cos\theta \tag{SI.4.1}$$

where σ_l is the liquid surface tension, θ is the contact angle, and σ_s is the substrate surface energy. Here, we assume that σ_s is approximately constant between trials, meaning that any changes in σ_{ls} are likely due to the liquid contributions; σ_s for glass is typically reported in the range of 50-100 mN/m.[17] Values for σ_l are measured via pendant drop analysis (as described in the Methods section); average σ_l values are reported in the main text.

The contact angle between droplet and substrate should be partially wetting as suggested by Dinic and Sharma[16]; insufficient spreading results in a large volume of fluid between the needle and substrate that forms a stable liquid bridge, as opposed to a bridge that self-thins.[18] To ensure the partially wetting criteria was met, the contact angle θ at the point of break-up was measured for each trial; in all cases, $\theta < 90°$ (Fig. S4). The average θ was less than 80° for each material, with a range of 60-80°.

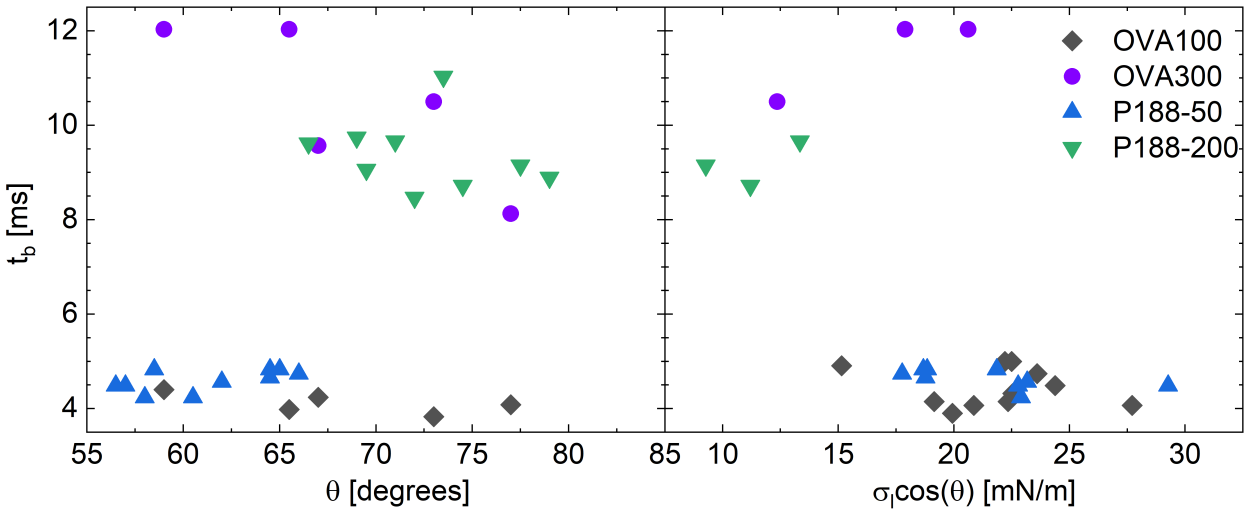

Figure S4: Breakup time t_b as a function of contact angle θ (a), and $\sigma_l cos\theta$ (b) for the high and low concentrations of OVA (100 and 300 mg/mL) and P188 (50 and 200 mg/mL). No trend in t_b is observed over the range of θ and $\sigma_l cos\theta$ values.

In Figure S4a, the lowest and highest concentrations of OVA and P188 are plotted with breakup time, t_b vs. θ. The two quantities do not appear correlated, indicating that any possible change in solid-liquid interfacial energy between trials does not impact the DoS results for this range of θ. Additionally, for the trials in which σ_l was measured, we find that the break-up time is independent of the $\sigma_l cos\theta$ contribution to Eqn. SI.4.1 (Figure S4b). Additionally, we see that the $\sigma_l cos\theta$ contribution values are overlapping for most of the low and high concentration data shown in Figure S4b, giving further confidence in the results.

SI.5 Dynamic light scattering (DLS)

Dynamic light scattering was used to confirm the size of structures present in dilute P188 and OVA solutions. Fig. S5 shows DLS results for 1 mg/mL OVA and corresponding raw auto-correlation curves, specifically the second order auto-correlation function, $g^{(2)}$. When describing OVA as Rayleigh spheres, the size distribution based on mass (and number) shows a primary peak at 2.8 nm (polydispersity = 10%) accounting for 99.9% of the mass, which compares favorably with literature reports of a hydrodynamic radius R_h of 2.9 nm.[19–22]

Note that a small contribution to the scattering by mass (0.1%), that is larger when examined by intensity, is observed around 30 nm (Fig. S5a); this peak corresponds to the small shoulder

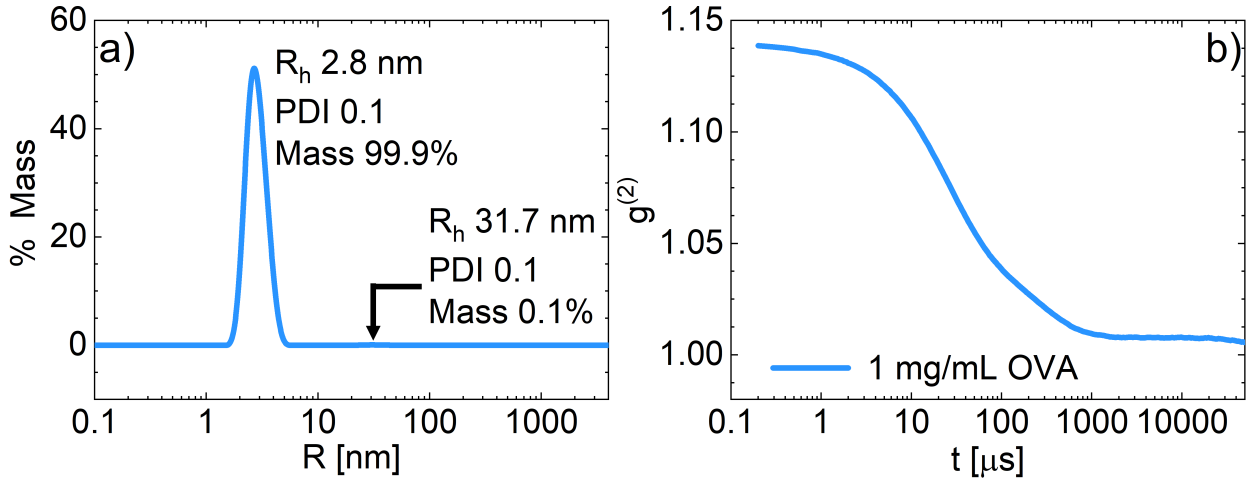

Figure S5: 1 mg/mL OVA DLS data a) mass size distribution with Rh, mass percentage and Polydispersity Index (PDI) of the peak, and b) raw autocorrelation curve.

observed in the decay curve at longer times ($\sim$100 μs, Fig. S6b). Due to the presence of this second population, a regularization fit that accounts for multiple populations was used to extract the size distributions. Complementary data on 0.5 mg/mL OVA taken on another instrument lacks this larger structure peak and gives the same hydrodynamic radius $R_h = 2.9$ nm (Fig. S6), suggesting that the primary peak fit in the first dataset is not impacted by the shoulder. Both datasets are shown for consistency, such that both OVA and P188 were measured on the same instrument.

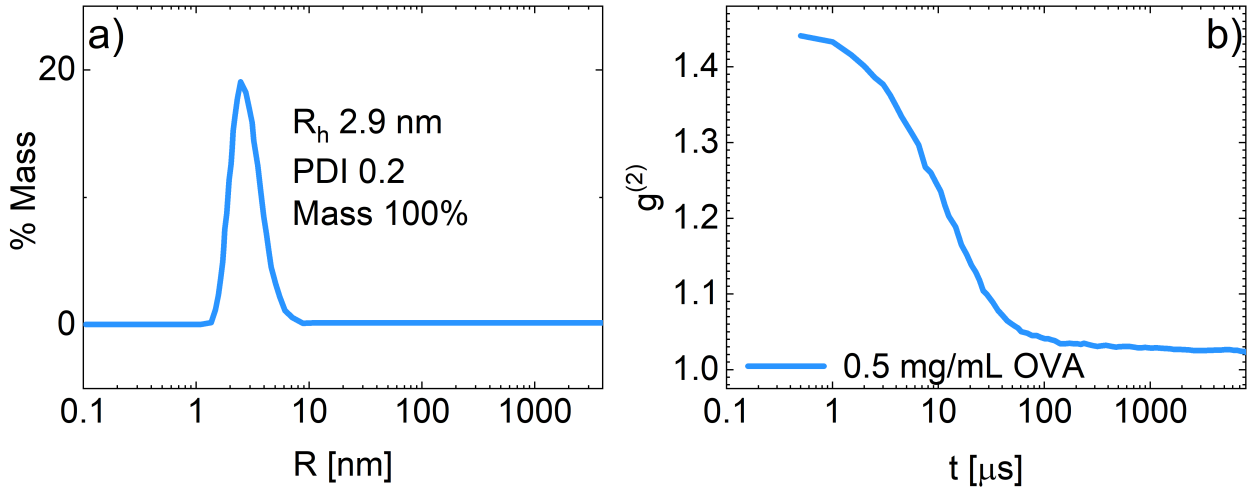

Figure S6: 0.5 mg/mL OVA DLS data measured on the Malvern Zetasizer, a) mass size distribution with R_h, mass percentage and Polydispersity Index (PDI) of each peak and b) raw autocorrelation curve.

Fig. S7 shows the DLS data for P188 solutions of 10 and 20 mg/mL, which are indistinguishable from one another. The average P188 R_h is determined assuming a coil conformation as

opposed to Rayleigh spheres, given that unimers are expected at these concentrations; however, no difference in R_h was observed if the Rayleigh sphere model was instead used. A single peak is observed for all trials, giving $R_h = 2.7$ nm (polydispersity = 10%) on both a mass and number basis, consistent with reported R_h for P188 unimers.[4,23,24]

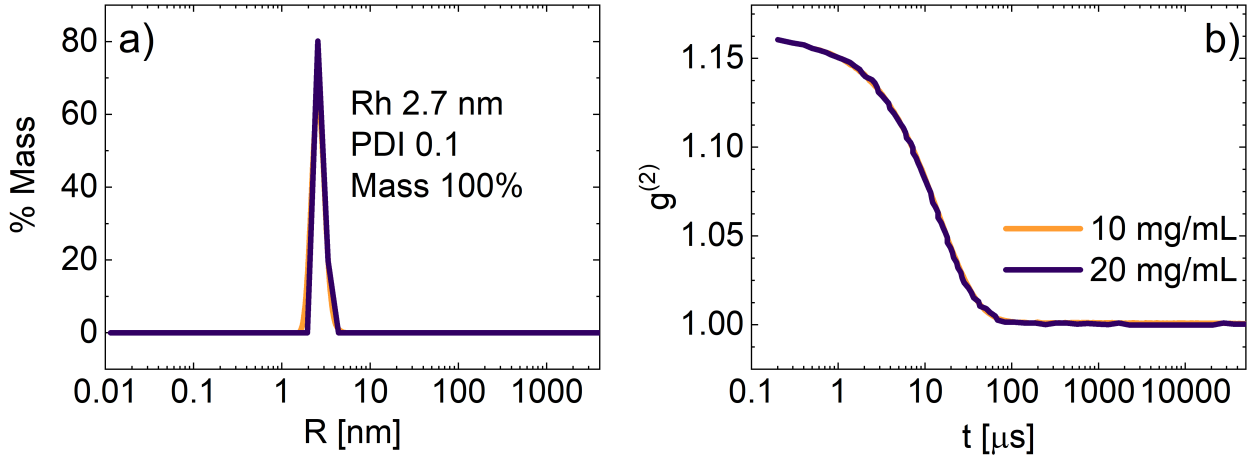

Figure S7: DLS data for 10-20 mg/mL P188, a) mass percentage and Polydispersity Index (PDI) of the peak, and b) raw autocorrelation curve.

Additional higher concentration P188 solutions were measured to determine if micelles or larger structures formed at any solution concentrations (Fig. S8). While the unimer peak is expected around $R_h = 2.5$ nm, the micelle size is expected to be ~7 nm.[24] While high quality data could not be obtained for concentrated P188 (200 mg/mL), no evidence of micelle formation is seen in the DLS data for concentrations of 100 mg/mL P188 and below (Fig. S8); all concentrations exhibit a single peak. The peak shifts to slightly smaller sizes with increasing concentration, which likely reflects the high solution concentration.

Solutions of 1:1 by mass P188:OVA were measured to assess whether the combined solutions formed large protein-poloxamer complexes. A solution of OVA1/P188-1 (Fig. S9) was used to determine the size of the species in solution. A primary peak of 2.8 nm (polydispersity = 10%) is observed, which is consistent with the similarly sized individual components. Higher concentrations of P188 and OVA solutions (50, 100 and 200 mg/mL of each component) were also measured. While these solutions were too concentrated to provide accurate size estimates, the measurements are useful for assessing an approximate level of aggregation and complexing in protein-poloxamer solutions. In the $g^{(2)}$ curves shown in Fig. S10b, a shoulder appears for the the OVA50/P188-50 and intensifies for the OVA100/P188-100 and OVA200/P188-200 samples. This shoulder indicates

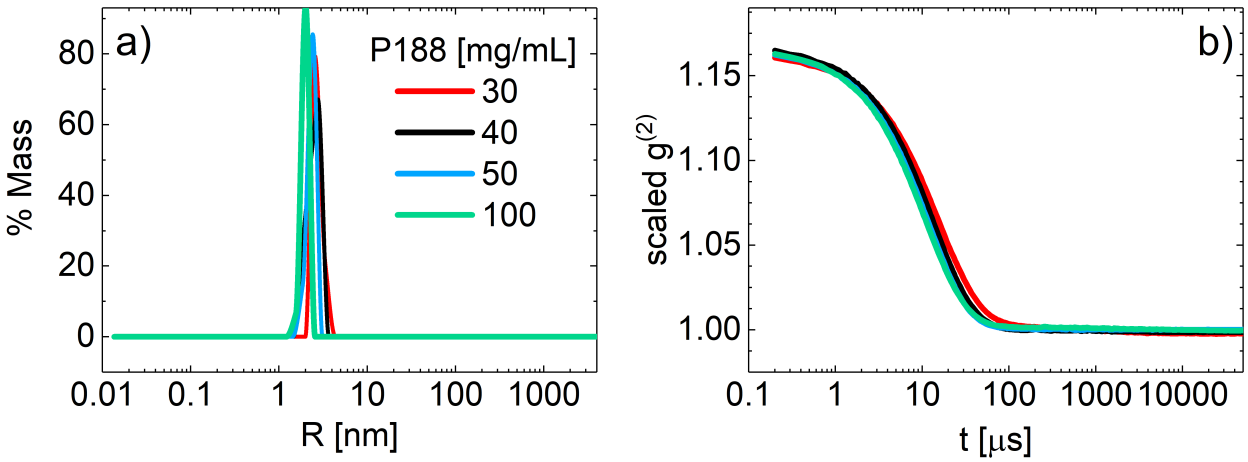

Figure S8: DLS data measured on P188 solutions from 30 through 100 mg/mL, a) mass size distribution and b) raw autocorrelation curves (scaled for comparison across samples).

the presence of larger complexes or interactions between components in solution, either of which could occur. However, even if this shoulder is assumed to correspond to a second population as opposed to interactions, the total mass percentage of this larger population is quite small. In fact, for OVA200/P188-200, which is a higher concentration than any of the solutions measured in DoS experiments, these potential larger size structures are less than 6% of the total mass (Table S10), indicating that these larger species do not dominate the solution behavior. Additionally, at lower times in Fig. S10b, the $g^{(2)}$ curves for all concentrations overlay, indicating that the smaller particles are similar in size across solutions.

Table S2: The mass % of the primary peak for 1:1 OVA P188 samples

Sample	Primary peak mass%
OVA1/P188-1	99.9
OVA50/P188-50	99.2
OVA100/P188-100	98.1
OVA200/P188-200	94.3

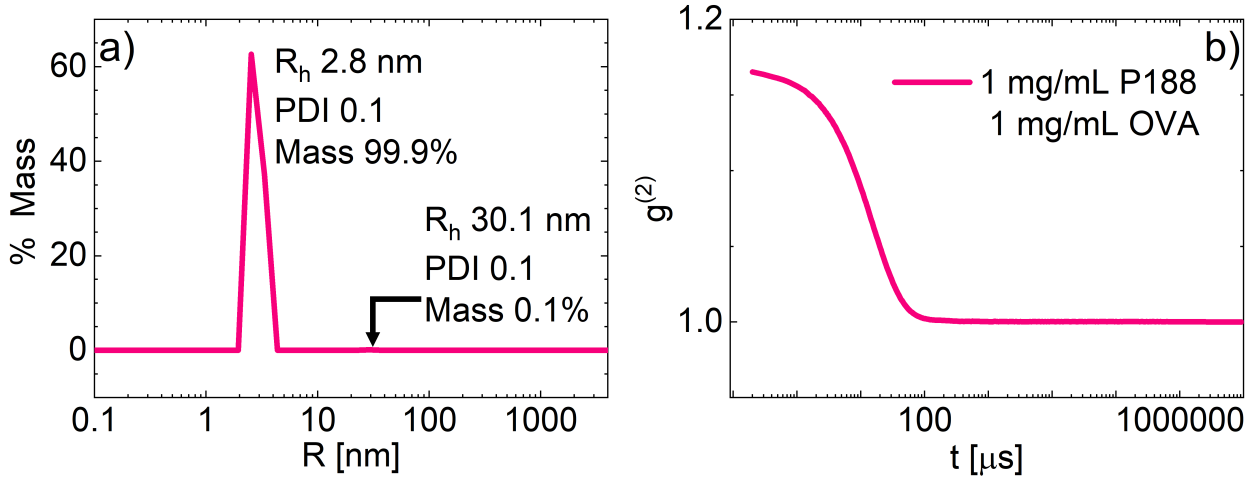

Figure S9: DLS data measured on a solution of 1 mg/mL each of P188 and OVA, a) mass size distribution and b) raw autocorrelation curves (scaled for comparison across samples). Note that in (a), the size distribution is shown to indicate the presence of one population; however, the extracted sizes are not accurate due to high solution concentration.

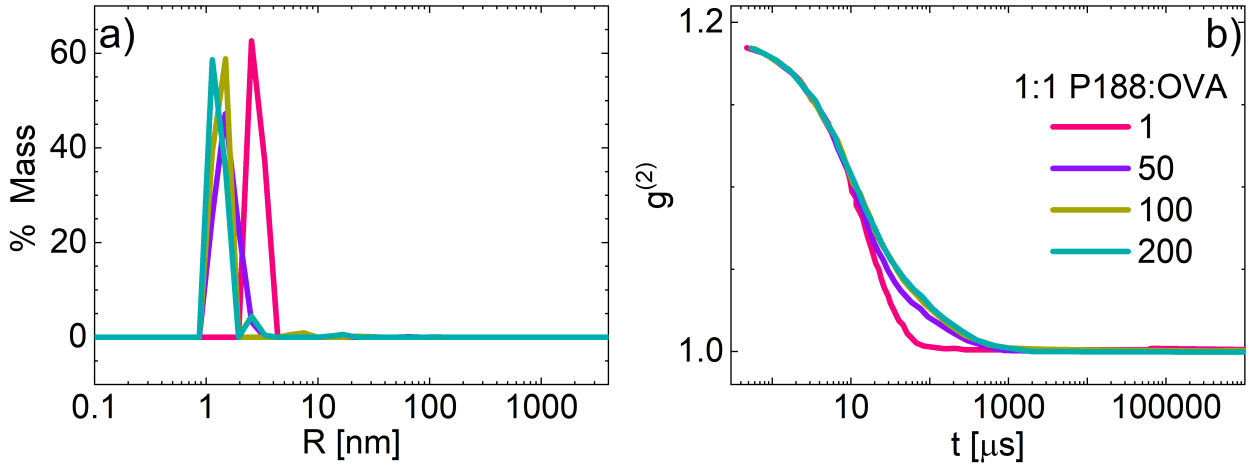

Figure S10: DLS data measured on a solution of 1, 50, 100, and 200 mg/mL each of P188 and OVA, a) mass size distribution and b) raw autocorrelation curves (scaled for comparison across samples).

SI.6 Prefactor α determination for inertiocapillary thinning

The prefactor for the inertiocapillary equation α is material and device dependent and found by previous work[25] to vary between 0.4-0.6. In Table S3, the value of α was allowed to vary such that the values of C_{calc} and C_{fit} were equal. In this work, a constant 0.6 was selected as the prefactor because this value of α is the average of the water, OVA100, P188-50, and OVA100/P188-50 (Table S3); these samples are the most dilute in each category of materials studied, and are thus most likely to exhibit IC behavior. As seen in Table S3, if α were allowed to vary for all samples instead of choosing a constant, α varies between 0.48 and 0.63 for most materials studied. Notable exceptions occur in the three samples that clearly deviate from IC behavior and are better described by the Anna-McKinley model for weakly elastic fluids (P188-200, OVA100/P188-200, OVA200/P188-100), providing additional support for employing this model.

Table S3: The prefactor α was allowed to vary to so that the C_{fit} and C_{calc} values matched for each material studied. α marked by † were selected as the α for that material. Samples marked by the ** symbols deviate from IC behavior and were fit with the Anna-McKinley empirical model for weakly elastic fluids.

sample	α	C_{calc} and C_{fit}
water	0.61	40.1
OVA100	0.60†	34.3
OVA200	0.57	31.2
OVA300	0.51	27.9
P188-50	0.54†	30.1
P188-100	0.54	29.2
P188-200**	0.68	37.2
OVA100/P188-50	0.62†	34.1
OVA100/P188-100	0.48	26.3
OVA100/P188-200**	2.28	120.3
OVA200/P188-100**	0.99	53.0

SI.7 Power law (PL) fits for weakly elastic thinning samples

To determine the appropriate fitting regime for samples eventually fit with the Anna-McKinley model for weakly elastic fluids, power law fits were performed to describe the behavior near the end of fitting (Figs. S11, S12). The behavior and associated PL for the most weakly elastic thinning sample, P188-200, vs. its lower concentration counterparts is shown in Fig. S11. As seen in Fig. S11a, lower concentration P188 solutions (50-100 mg/mL) follow IC behavior, indicated by the

single power law fit describing the full data range (black solid lines). That a single exponent of $n \approx 2/3$ can describe the entire dataset is consistent with IC behavior and the reported values for n and n_0 in Table 1 in the main text, which are not significantly different.

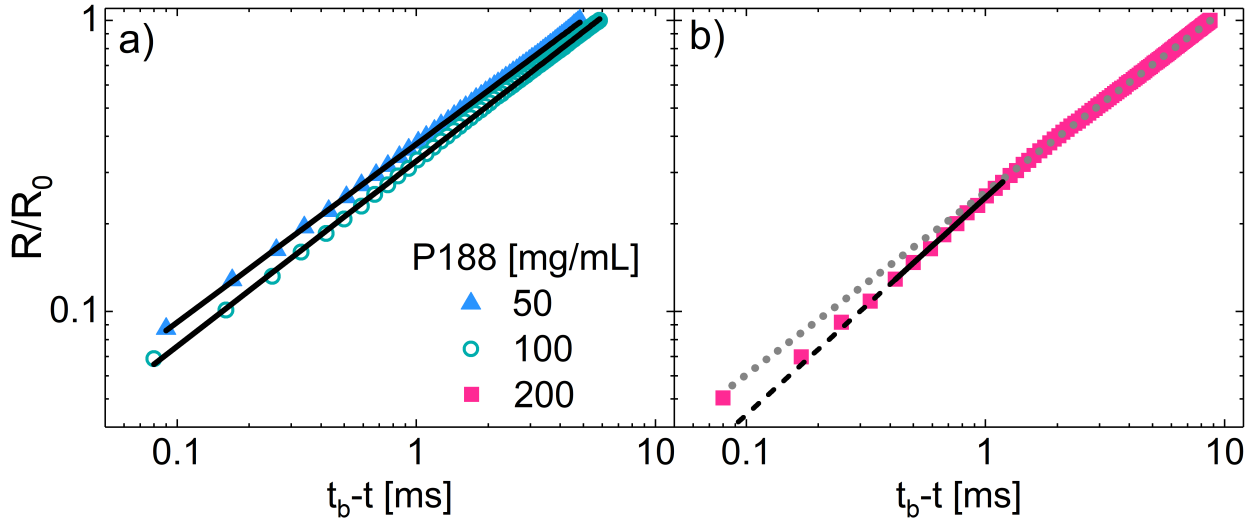

Figure S11: Log-log plot of $t_b - t$ vs. R/R_0 for P188 solutions following IC behavior (a) and those deviating from IC/PL (b). Black solid lines describe the end of thinning, n, but are extended over the full dataset in (a), indicating that a single exponent can describe the behavior. In (b), neither n nor n_0 fits (gray dashed line) can fully describe the dataset. The black dashed lines show the n fit extended beyond the fit region, indicating n does not fully describe the end of thinning, similar to that shown by Dinic and Sharma.[26]

Fig. S11b shows the thinning data for P188-200, which deviates from both IC and PL behavior as neither n nor n_0 fits can fully describe the dataset. Here, the fits for the initial thinning index n_0 (gray dashed line) are extended over the full data range so the second thinning region can be easily detected; no clear second regime exists at lower concentrations (Fig. S11a). PL fits to the second thinning regime are shown with the black solid line, where the fit region begins near the deviation from the n_0 fit and extends until the fit residuals are no longer randomly distributed. While the Anna-McKinley model does describe the end of thinning well (see main text), the black dashed lines in Fig. S11b show the n fit extended beyond the fit region, indicating the PL fit for n does not fully describe the end of thinning. This behavior is similar to the deviations from PL behavior shown by Dinic and Sharma, which was one piece of evidence used to justify use of the Anna-McKinley model.[26] Additionally, if the PL fit is used for P188-200, $n = 0.77 \pm 0.02$, which would indicate a transition towards more viscous behavior. However, as shown in Table S1 and Fig. S1, Oh is still far below 1 ($Oh \sim 0.09$) and this solution exhibits nearly Newtonian behavior,

suggesting that the n value extracted from these fits is not physically meaningful.

A similar analysis was performed for the two 300 mg/mL protein/excipient solutions, OVA100/P188-200 and OVA200/P188-100 (Fig. S12b,c); the two lower concentration protein/excipient solutions did not exhibit deviations from IC/PL behavior (Fig. S12a). In OVA100/P188-200 (Fig. S12b), the initial thinning index $n_0 = 0.56 \pm 0.03$ is dramatically different from the final thinning index $n = 0.99 \pm 0.03$, which nears unity. While shear viscosity data is not available for the combined solutions, the viscosity values reported for the single-component formulations in Table S1 suggest that the Oh number for OVA100/P188-200 is also far below unity, and thus viscocapillary behavior with $n = 1$ would not be expected for this solution. As seen in Fig. S12b, the last several points (short $t_b - t$) in the radial decay curves do not follow PL behavior well, which is similar to but more dramatic than the deviations observed for P188-200 in Fig. S11b. Similar deviations are observed for OVA200/P188-100 (Fig. S12c), where $n_0 = 0.46 \pm 0.01$ and $n = 0.80 \pm 0.03$. While not as dramatic as in OVA100/P188-200, clear deviations from the fit n PL behavior are observed at short $t_b - t$. The deviation from PL behavior for both of these solutions is visually supported by the thin filament observed at the end of thinning that is characteristic of weakly elastic behavior. The Anna-McKinley models fit shown in the results section of the main text represent a better fit of the entire end thinning behavior for both concentrated protein/excipient solutions.[26,27]

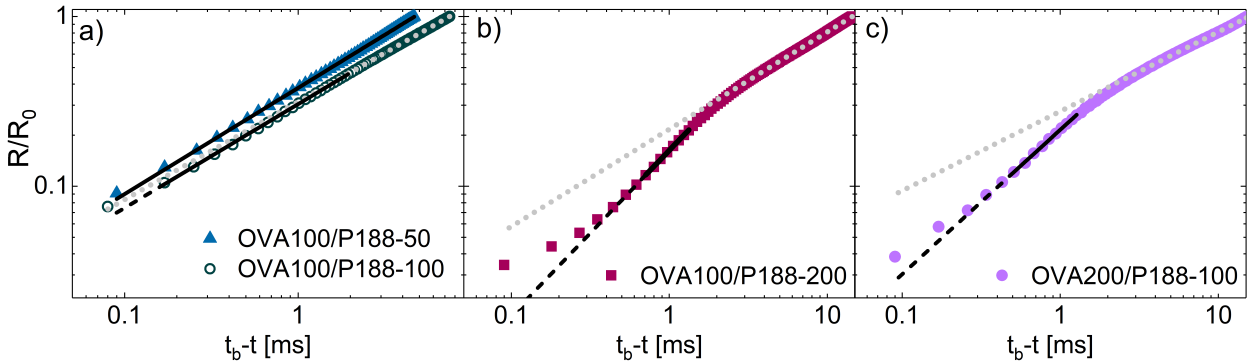

Figure S12: Log-log plot of $t_b - t$ vs. R/R_0 for OVA/P188 solutions following approximately IC behavior (a) and those deviating from IC/PL (b). Black solid lines describe the end of thinning, n. In (a), a single power law can describe OVA100/P188-50, whereas two power laws of similar index describe OVA100/P188-100. In the concentrated protein/excipient solutions (b,c), neither n nor n_0 fits (gray dashed line) can fully describe the dataset. The black dashed lines show the n fit extended beyond the fit region, indicating n does not fully describe the end of thinning, similar to that shown by Dinic and Sharma.[26]

SI.8 Anna-McKinley sample fits

To better show the weakly elastic thinning behavior for concentrated solutions containing P188, data is shown on a linear scale (zoomed in at end of thinning behavior) in Figs. S13-S14. In Fig. S13a, a representative trial is shown for OVA100/P188-200, where a clear change in behavior exhibiting a concave up curvature corresponds to weak elasticity. While deviations from PL fitting were used to select the fit ranged for each trial, Fig. S13b shows the Anna-McKinley fits for various data ranges near the end of thinning, with corresponding vertical lines indicating the lowest fit time for each dataset. As seen in the inset, the extracted rheological parameters are robust to these large changes in fitting range, giving confidence in the extracted parameters.

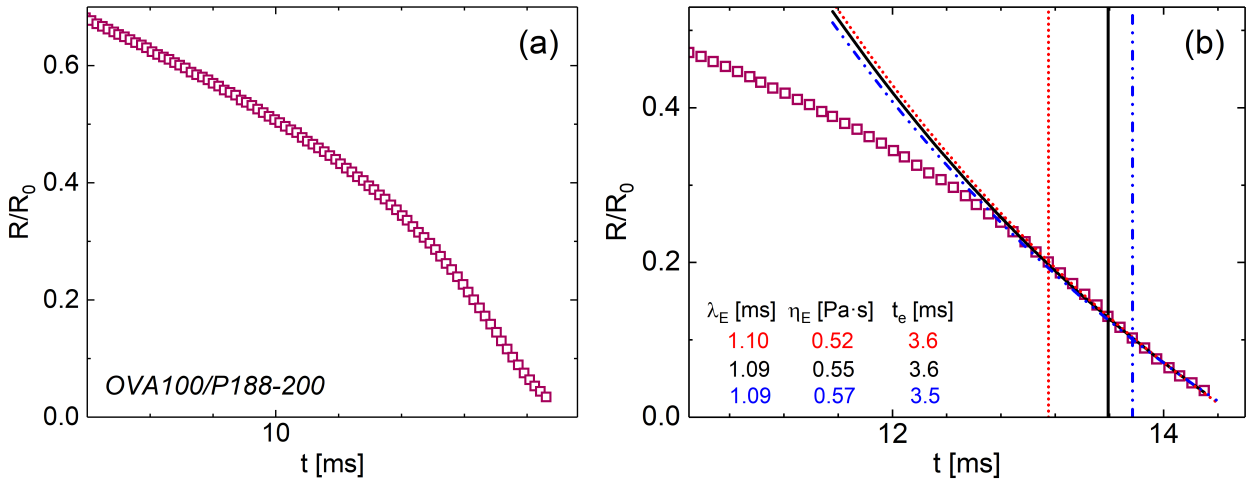

Figure S13: a) Representative end of thinning behavior for OVA100/P188-200, zoomed in and shown on a linear scale so the weakly elastic region (concave up curvature) can be clearly seen. b) While deviations from PL behavior were used to select the fitting range for the Anna-McKinley model fits, extracted parameters are robust to choice of fit range. Vertical lines indicate the lowest time fit for each data range.

A similar analysis is performed for the other weakly elastic samples, OVA200/P188-100 and P188-200 (Fig. S14). As shown in Fig. S14a, when the end thinning regions are compared for OVA100/P188-200 vs. OVA200/P188-100, the elastic region is longer in duration for OVA100/P188-200. This longer duration elastic region is reflected in the elastic filament time, t_e, extracted from the model, which is longer in OVA100/P188-200. Fig. S14b shows two fitting ranges for OVA200/P188-100 and associated fits, which are nearly identical. As such, the extracted fit values are also nearly identical. Finally in Fig. S14, two fitting ranges are compared for P188-200. The greatest difference in the model fits and extracted parameters is observed in this sample, due to the fact that the weakest elastic behavior is observed here, which leads to few points in the fitting

region. To combat this uncertainty, a large number of trials was performed for P188-200.

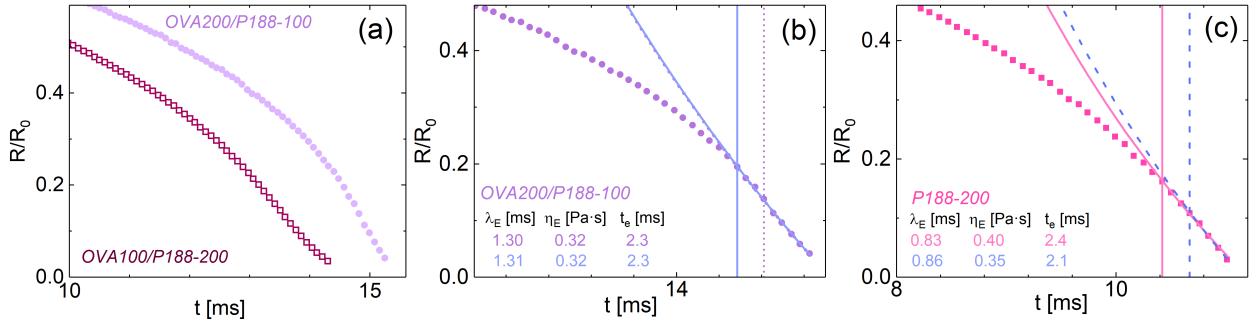

Figure S14: a) Representative end of thinning behavior for OVA100/P188-200 vs. OVA200/P188-100, zoomed in and shown on a linear scale so the weakly elastic region (concave up curvature) can be clearly seen. A shorter time elastic region is seen in OVA200/P188-100, which is reflected in values for the elastic filament lifetime extracted with the Anna-McKinley model. While deviations from PL behavior were used to select the fitting range, extracted parameters for b) OVA200/P188-100 and c) P188-200 are robust to choice of fit range. Vertical lines indicate the lowest time fit for each data range.

SI.9 Raw data and reproducibility for DoS trials

DoS trials were repeated a minimum of 5 times ($N = 5$, Figs. S15–S17). When reporting statistics such as break-up time or n, uncertainty was calculated by averaging the results from all trials at that concentration of OVA and/or P188 and reporting the 95% confidence interval based on those trials. While fit uncertainty arises in PL and Anna-McKinley model fitting, model fitting uncertainties were less than the average error between trials and are thus not reported.

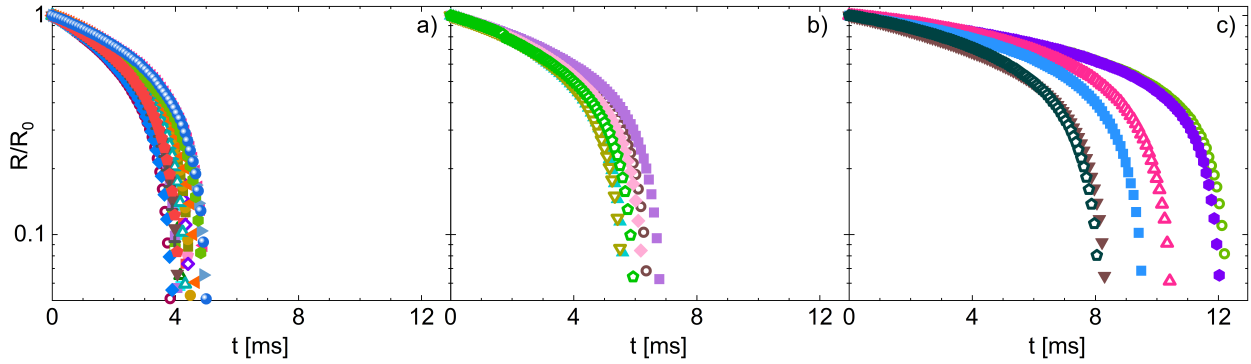

Figure S15: Entirety of the ovalbumin trials for a) 100 mg/mL OVA (21 trials), b) 200 mg/mL OVA (6 trials), and c) 300 mg/mL (6 trials).

Figs. S15, S16, and S17 show all trials for OVA, P188, and OVA/P188, respectively, demonstrating the reproducibility of the DoS measurements. In general, the spread of breakup times t_b increases with total solution concentration, as seen in Fig. S15c for OVA300, in Fig. S16c for P188-200, and in Fig. S17c,d for the 300 mg/mL OVA/P188 solutions. While the variation be-

tween trials generally increases as concentration increases, the 95% confidence interval is less than 10% of the average break-up time for all concentrations studied.

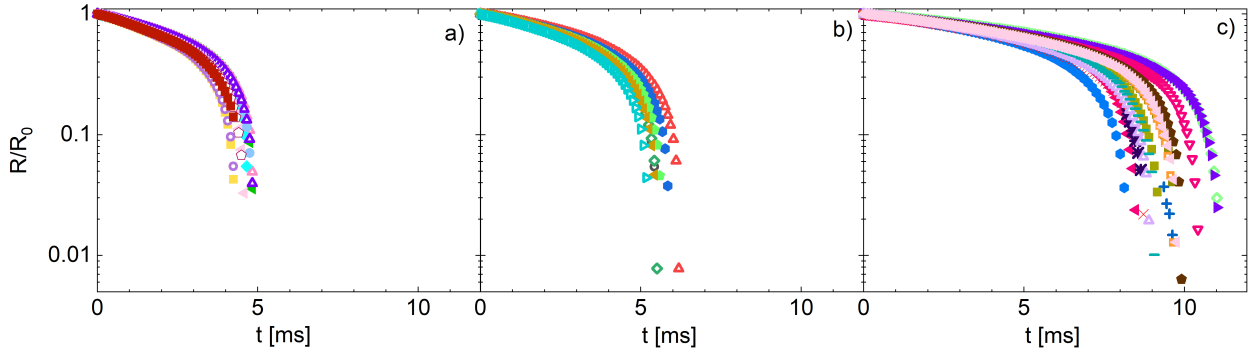

Figure S16: Entirety of the P188 trials, for a) 50 mg/mL P188 (10 trials), b) 100 mg/mL P188 (7 trials), and c) 200 mg/mL P188 (15 trials).

In addition to obtaining a narrow distribution of breakup times between trials performed on the same day and on the same sample preparation, many of the replicate trials were performed on different days using newly prepared samples. For example, the two 300 mg/mL OVA trials in Fig. S15c with breakup times occuring at ∼8 ms were from two different samples taken on two different days; the 10 trials shown for 50 mg/mL P188 in Fig. S16a trials were also taken on two separate days using different sample batches. As these differences did not appear to affect the radial decay profiles, the results are robust over multiple trials, sample preparations, and laboratory conditions.

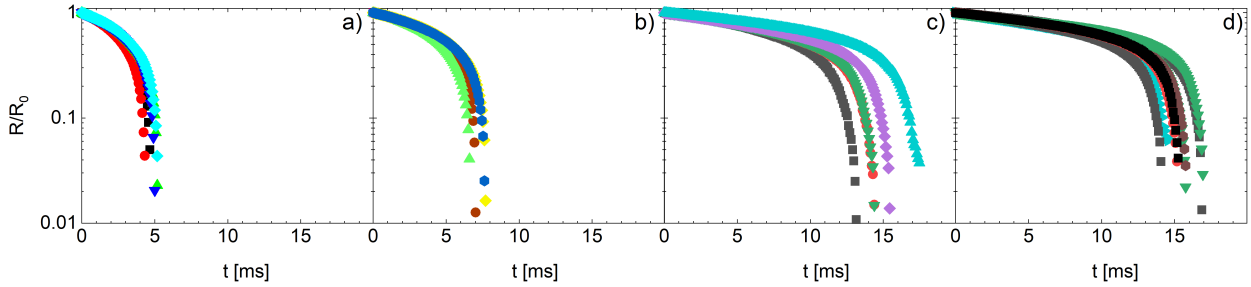

Figure S17: Entirety of the trials for combined P188/OVA, for a) OVA100/P188-50 (5 trials), b) OVA100/P188-100 (5 trials), c) OVA100/P188-200 (5 trials), and d) OVA200/P188-100 (8 trials).

SI.10 Direct comparison of 200 mg/mL solutions

Fig. S18 shows the break-up behavior of OVA, P188, and OVA/P188 each containing 200 mg/mL of solute. OVA200 (t_b=6.1 ± 0.4) and OVA100/P188-100 (t_b=7.3 ± 0.3) have similar break-up times and filament shape at breakup, although the OVA100/P188-100 solution thins over slightly longer timescales. In comparison, the P188-200 has a thinner, more cylindrical filament indicative

of weakly elastic behavior. When compared with the results from OVA200/P188-100, these results suggest that the emergence of weakly elastic behavior likely requires a combination of a minimum P188 concentration and minimum solution concentration, and that the thinning behavior is not determined entirely by the amount of solute.

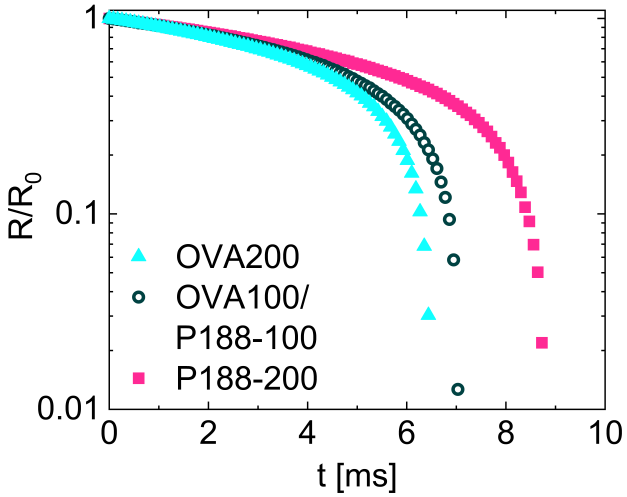

Figure S18: a) R/R_0 vs. time for OVA200, OVA100/P188-100, and P188-200. Each solution has 200 mg/mL of solute, but only the OVA and combined solution exhibit similar behavior.

SI.11 Extension rates experienced by sample

To add further evidence that increasing the solute concentration leads to deviations from IC thinning, the extension rates during thinning were calculated for all materials and concentrations (Fig. S19). Calculation of the extension rates also confirms that the samples are experiencing extension rates relevant to clinical injections ($\sim 10^5$ s^{-1} [28]). Here, we presume that once normalized appropriately, solutions exhibiting IC thinning will show comparable extension rate profiles, whereas deviations will be seen for higher concentration solutions.

The Hencky strain and strain rate are defined as:

$$\epsilon = 2 \ln \left(\frac{R_0}{R} \right) \tag{SI.11.1}$$

$$\frac{\mathrm{d}\epsilon(t)}{\mathrm{d}t} = -\frac{2}{R_{\text{min}}(t)} \frac{\mathrm{d}R_{\text{min}}(t)}{\mathrm{d}t} \tag{SI.11.2}$$

In Fig. S19, the extension rates shown were normalized by the time where R/R_0=0.05 (values were interpolated between the two closest points if necessary). The R/R_0=0.05 normalization was

chosen as a point near the end of break-up since not all of the trials ended at the same R/R_0. Fig. S19a shows the extension rates for the materials that show little if any deviation from IC thinning; when normalizing the trial time by the break-up time in Fig. S19a, the IC liquids nearly overlay with water. Each of these solutions exhibits similar extension rates to water and similar shapes in the evolution of the extension rate. However, the slopes of the extension rate evolution deviate from the samples exhibiting IC behavior for the fluids shown in Fig. S19b, further supporting that these fluids are in a different flow regime. Additionally in Fig. S19b, the higher concentration materials, OVA300, P188-100, P188-200, and OVA100/P188-100, despite having longer total breakup times, the total time spent at high extension rates (defined as $\geq 10^3$ s^{-1}) is similar to the IC fluids at $\sim$1.3 ms. The OVA100/P188-200 solution however, spends 15% longer at high extension rates than the other fluids studied.

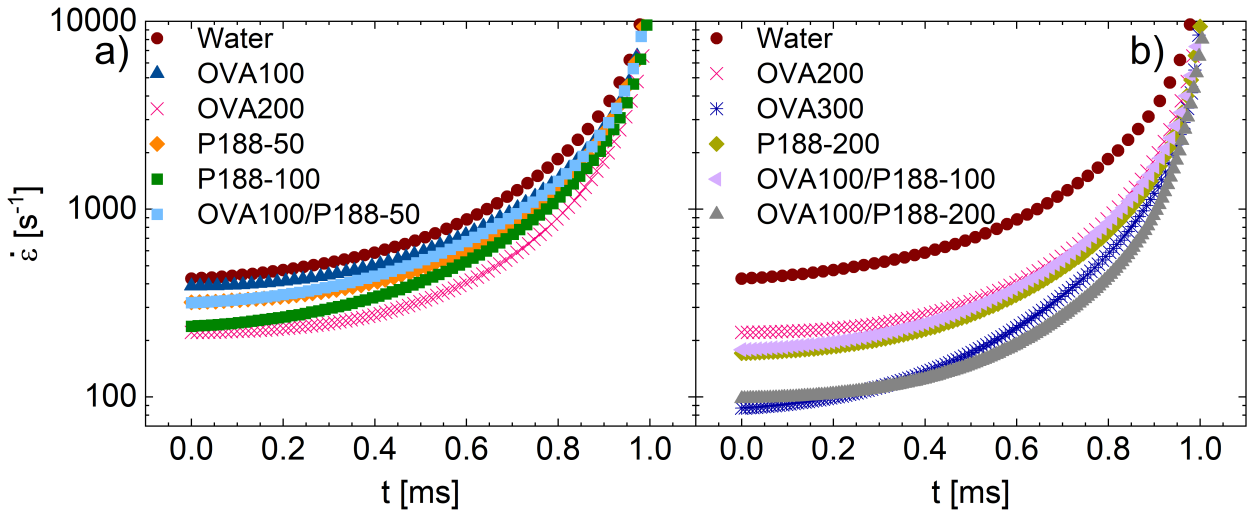

Figure S19: The extension rates for water, OVA, P188 and combined solutions are shown. a) Materials exhibiting IC or nearly IC behavior. b) Higher concentration solutions that deviate from IC behavior.

References

[1] K. Monkos, *Biophys. Chem.*, 2000, **85**, 7–16.

[2] M. Brust, C. Schaefer, R. Doerr, L. Pan, M. Garcia, P. Arratia and C. Wagner, *Phys. Rev. Lett.*, 2013, **110**, 078305.

[3] P. J. McCauley, S. Kumar and M. A. Calabrese, *Langmuir*, 2021.

[4] P. Alexandridis, J. F. Holzwarth and T. A. Hatton, *Macromolecules*, 1994, **27**, 2414–2425.

[5] C. Clasen, *Korea-Aust. Rheol. J.*, 2010, **22**, 331–338.

[6] T. S. Kumar, V. Prasad and M. Pandit, *J. Biochem. Biophys. Methods*, 1994, **28**, 243–247.

[7] B. T. Kurien and R. H. Scofield, *Protein Electrophoresis*, Springer, 2012, pp. 633–640.

[8] D. A. Omana and J. Wu, *J. Agric. Food Chem*, 2009, **57**, 3596–3603.

[9] V. Raikos, R. Hansen, L. Campbell and S. R. Euston, *Food Chem.*, 2006, **99**, 702–710.

[10] S. K. Cooke and H. A. Sampson, *J. Immunol.*, 1997, **159**, 2026–2032.

[11] C. Desert, C. Guerin-Dubiard, F. Nau, G. Jan, F. Val and J. Mallard, *J. Agric. Food Chem*, 2001, **49**, 4553–4561.

[12] E. Holen and S. Elsayed, *Int. Arch. Allergy Immunol.*, 1990, **91**, 136–141.

[13] S. Abeyrathne, H. Lee and D. U. Ahn, *Iowa State University Animal Industry Report*, 2016, **13**, 1001–1009.

[14] T. Croguennec, F. Nau, S. Pezennec and G. Brule, *J. Agric. Food Chem*, 2000, **48**, 4883–4889.

[15] M. M. Pereira, R. A. Cruz, M. R. Almeida, Á. S. Lima, J. A. Coutinho and M. G. Freire, *Process Biochem.*, 2016, **51**, 781–791.

[16] J. Dinic, Y. Zhang, L. N. Jimenez and V. Sharma, *ACS Macro Lett.*, 2015, **4**, 804–808.

[17] S.-C. Weng, A. Y.-G. Fuh, F.-C. Tang and K.-T. Cheng, *Liquid Cryst.*, 2016, **43**, 1221–1229.

[18] L. A. Slobozhanin and J. M. Perales, *Phys. of Fluids A-Fluid*, 1993, **5**, 1305–1314.

[19] Y.-T. Xu, Y.-H. Wang, F.-P. Chen and C.-H. Tang, *Food Hydrocoll.*, 2020, **103**, 105694.

[20] J. Liu, J. Liu and X. Zhang, *Int. J. Food Eng.*, 2012, **8**, 1–12.

[21] J. Stetefeld, S. A. McKenna and T. R. Patel, *Biophys. Rev.*, 2016, **8**, 409–427.

[22] S. Schneider, *Agilent Technologies Application*, 2014.

[23] Z. Zhou and B. Chu, *J. Colloid Interface Sci.*, 1988, **126**, 171–180.

[24] U. Adhikari, A. Goliaei, L. Tsereteli and M. L. Berkowitz, *J. Phys. Chem. B*, 2016, **120**, 5823–5830.

[25] A. Deblais, M. Herrada, I. Hauner, K. P. Velikov, T. Van Roon, H. Kellay, J. Eggers and D. Bonn, *Phys. Rev. Lett.*, 2018, **121**, 254501.

[26] J. Dinic and V. Sharma, *Macromolecules*, 2020, **53**, 3424–3437.

[27] S. L. Anna and G. H. McKinley, *J. Rheol.*, 2001, **45**, 115–138.

[28] I. B. Bekard, P. Asimakis, J. Bertolini and D. E. Dunstan, *Biopolymers*, 2011, **95**, 733–745.